Archives of Biochemistry and Biophysics 776 (2026) 110693

Contents lists available at ScienceDirect

Archives of Biochemistry and Biophysics

journal homepage: www.elsevier.com/locate/yabbi

Nucleotide-dependent structural dynamics and domain motion in *Coxiella burnetii* EngA GTPases: Insights from molecular dynamics simulation

K.M. Kavya [a], Guruswaroop C [a], Upendra N [b], Krishnaveni S [a,*]

[a] Department of Studies in Physics, University of Mysore, Mysuru, India
[b] Center for Research and Innovations, Faculty of Natural Sciences, Adichunchanagiri University, B.G.Nagara, India

A B S T R A C T

EngA, a ribosome-associated bacterial GTPase essential for 50S subunit maturation and bacterial growth, lacks a human ortholog, making it an attractive antibacterial target. Its activity is governed by a nucleotide-dependent molecular switch: GTP binding promotes EngA association with the immature 50S subunit and facilitates rRNA processing, whereas GTP hydrolysis to GDP triggers dissociation from the ribosome. Structural studies on *Bacillus subtilis* EngA revealed that GTP-analog-bound EngA disrupts the GD1-KH interface required for 45S subunit association, while GDP-bound EngA retains these interactions. However, the molecular mechanism by which nucleotides regulate these transitions and whether similar mechanisms exist in other pathogenic species remain unclear. To address this, 1000 ns molecular dynamics simulations of *Coxiella burnetii* EngA was performed in four nucleotide-bound states: [GDP:GDP], [GDP:GTP-Mg^{2+}], [GTP-Mg^{2+}:GDP], and [GTP-Mg^{2+}:GTP-Mg^{2+}]. Analyses of principal components, interaction energies, and distance-angle parameters revealed nucleotide-dependent domain dynamics. In the [GTP-Mg^{2+}:GTP-Mg^{2+}] state, GD1 and KH domains moved apart, forming an open conformation, while in [GDP:GDP] they approached each other, forming a closed conformation consistent with cryo-EM structures. Community network analysis further showed that GDP binding to GD1 extends connectivity from the nucleotide to SwI, stabilizing SwI-KH interactions and restricting GD1 motion. In contrast, GTP-Mg^{2+} binding disrupts this network, enabling SwI-GD2 interactions that weaken the GD1-KH interface and promote an open conformation. Overall, the results highlight how nucleotide charge-dependent interactions regulate EngA allosteric network and drive its conformational switching mechanism.

1. Introduction

GTPases are molecular switches that cycle between two distinct conformations: an active GTP (Guanosine triphosphate) bound state and an inactive GDP (Guanosine diphosphate) bound state [1,2]. This nucleotide-dependent switching mechanism underlies their crucial role in diverse cellular processes, including cell proliferation, growth, protein translation, translocation, signal transduction, and ribosome biogenesis [3]. GTPases involved in ribosome maturation are termed ribosome assembly GTPases (RA-GTPases). They facilitate ribosomal maturation through protein recruitment, promote rRNA processing and folding to ensure proper subunit assembly, and mediate interactions between the 30S and 50S subunits [4]. In addition, RA-GTPases act as checkpoints by binding to immature 30S or 50S subunits, thereby preventing their premature association until both subunits are fully matured [5]. The RA-GTPases RbgA, ObgE, YsxC, and YphC are involved in the maturation of the 50S subunit, whereas RsgA, Era, and YqeH contribute to the maturation of the 30S subunit. EngA, YihA, and Obg help in the biogenesis of both the 30S and 50S subunits [6,7].

EngA (also known as Der, double-Era-like GTPase) is a broadly conserved bacterial RA-GTPase that is distinct from other RA-GTPases due to its two tandem GTP-binding domains. (GD1:G-domain I and GD2:G-domain II) (Fig. 1) [8]. These domains are followed by a C-terminal K-homology (KH) domain, which mediates RNA binding and plays a critical role in EngA-50S subunit interaction and assembly [9]. The G-domains bind nucleotides through their conserved G-motifs (G1-G5), with the G2 (threonine, T) motif coordinating the Mg^{2+} ion, and the G3 (aspartate-X-X-glycine, DXXG) motif coordinating both the Mg^{2+} ion and the γ-phosphate of GTP. Upon GTP hydrolysis, the γ-phosphate is released, causing conformational changes in the G2 and G3 loops, known as Switch I (SwI) and Switch II (SwII), respectively, thereby switching EngA from its active (on) state to its inactive (off) state [10,11].

The association of EngA with the ribosome is dictated by the nucleotide-bound state. In the [GTP:GTP] bound state, where both GD1 and GD2 are GTP-bound, EngA associates with the 50S ribosomal subunit. In the [GDP:GTP] state, with GDP bound to GD1 and GTP bound to GD2, EngA associates with the 30S, 50S, and 70S subunits [12]. In contrast, in the [GDP:GDP] state, where both domains are GDP-bound, EngA dissociates from the ribosomal subunit [12]. The nucleotide

* Corresponding author.
E-mail address: sk@physics.uni-mysore.ac.in (K. S).

https://doi.org/10.1016/j.abb.2025.110693
Received 8 October 2025; Received in revised form 2 December 2025; Accepted 3 December 2025
Available online 4 December 2025

dependency of EngA ribosome interactions may be attributed to conformational changes induced by GTP or GDP binding [13].

Interestingly, the crystal structures of *B. subtilis* EngA in different nucleotide-bound states ([GDP:GDP] and [Apo:GMPPNP]) do not exhibit major conformational differences (PDB ID: 4DCU and 5M7H) (Fig. S1). In contrast to the crystal structures, electron microscopy structures of ribosome-bound EngA (PDB ID: 9BS0, 3J8G) in the GTP analog GMPPNP bound state revealed major conformational changes compared to the crystal structures (Fig. 2). In the crystal structure, GD1 interacts closely with the KH domain (Fig. 2A), whereas in electron microscopy structure of ribosome-bound EngA (both *E. coli* and *B. subtilis*), GD1 is displaced away from the KH domain (Fig. 2B, C, and 2D). SAXS data further supported these observations, showing that EngA in the apo or GDP-bound form adopts an "off" conformation with a closed GD1-KH interface, resembling *B. subtilis* EngA crystal structure (PDB IDs: 2HJG and 4DCU). In contrast, the presence of GTP analogs induced a distinct quaternary rearrangement, disrupting the GD1-KH interface. This rearrangement represents an intermediate state between the EngA apo/GDP "off" state and the ribosome-bound "on" states. Overall, nucleotide-mediated conformational changes appear to facilitate EngA association with the 50S ribosomal subunit [9,14].

These structural comparisons provide insights into the "on" and "off" states of EngA; however, the precise role of nucleotide binding in driving these conformational changes remains unclear. Furthermore, it is unknown whether similar nucleotide-dependent transitions occur in EngA from other species. To address this, the crystal structures of EngA from *B. subtilis* (PDB ID: 4DCU), *Coxiella burnetii* (*C. burnetii,* PDB ID: 5DN8), *Thermotoga maritima* (*T. maritima,* PDB ID: 1MKY), and *Neisseria gonorrhoeae* (*N. gonorrhoeae,* PDB ID: 6XRS) were superimposed. Despite all EngA structures bound to GDP nucleotide, the GD1 domain adopts different orientations across species when aligned using the GD2-KH region as a reference (Fig. S2). Although the GD1 orientation varies, all structures show an interaction between the GD1 and KH domains (Fig. 3 and Table S1), referred to as the GD1-KH interface. However, this interface does not involve the same regions of the GD1 and KH domains across species.

The presence of the GD1-KH interaction across species in the GDP-bound state raises the question of whether this interface is similarly disrupted in the GTP-bound form of EngA, as observed in the ribosome-bound *B. subtilis* EngA structure (GTP-analog bound). However, this cannot be verified because ribosome-bound EngA structures for *C. burnetii*, *T. maritima*, and *N. gonorrhoeae* species are not available. This motivated us to explore whether EngA from other species undergoes nucleotide-associated conformational transitions similar to those of *B. subtilis* EngA and how nucleotide binding regulates these dynamic changes. Among the available EngA crystal structures, *C. burnetii* EngA was selected for this study. *C. burnetii* is a pathogenic bacterium responsible for Q fever, which can range from an acute flu-like illness to chronic endocarditis [15]. Although antibiotics such as doxycycline remain effective against acute Q fever, the emergence of antibiotic-resistant strains and the difficulty in treating chronic infections underscore the need for alternative therapeutic strategies [16]. EngA, an essential prokaryotic GTPase critical for ribosome biogenesis, represents a promising target since its malfunction disrupts bacterial growth and survival. Importantly, humans lack EngA homologs, making it possible to design antibacterial agents that selectively inhibit bacterial EngA without interfering with human GTPase activity [17]. To use EngA as a drug target, it is necessary to elucidate how its structural dynamics are regulated by different nucleotide-bound states and how these transitions govern its shift between active ("on") and inactive ("off") conformations.

Therefore, to gain insights into the nucleotide-dependent "on" and "off" states of EngA, and to understand how nucleotide binding regulates these transitions, we performed molecular dynamics (MD) simulations

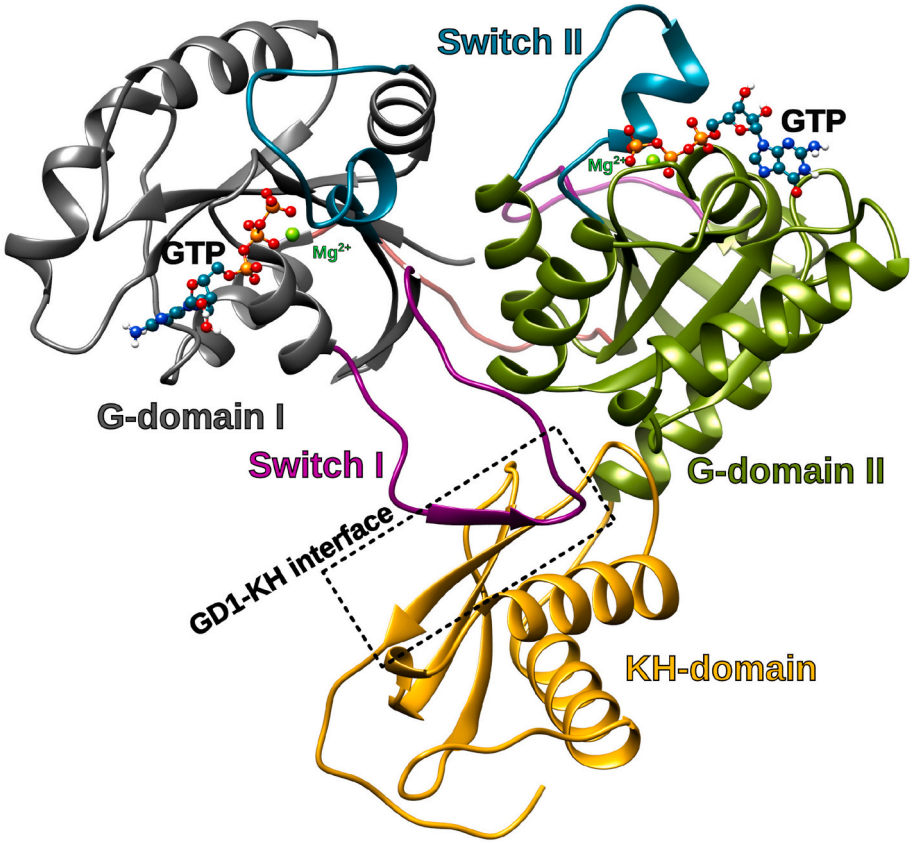

Fig. 1. Ribbon representation of *Coxiella burnetii* EngA protein structure (PDB ID: 5DN8), consisting of G-domain I (residues 1–162) with Switch I and Switch II, linker (residues 163–175), G-domain II (residues 176–349) with Switch I and Switch II, and KH-domain (residues 353–443).

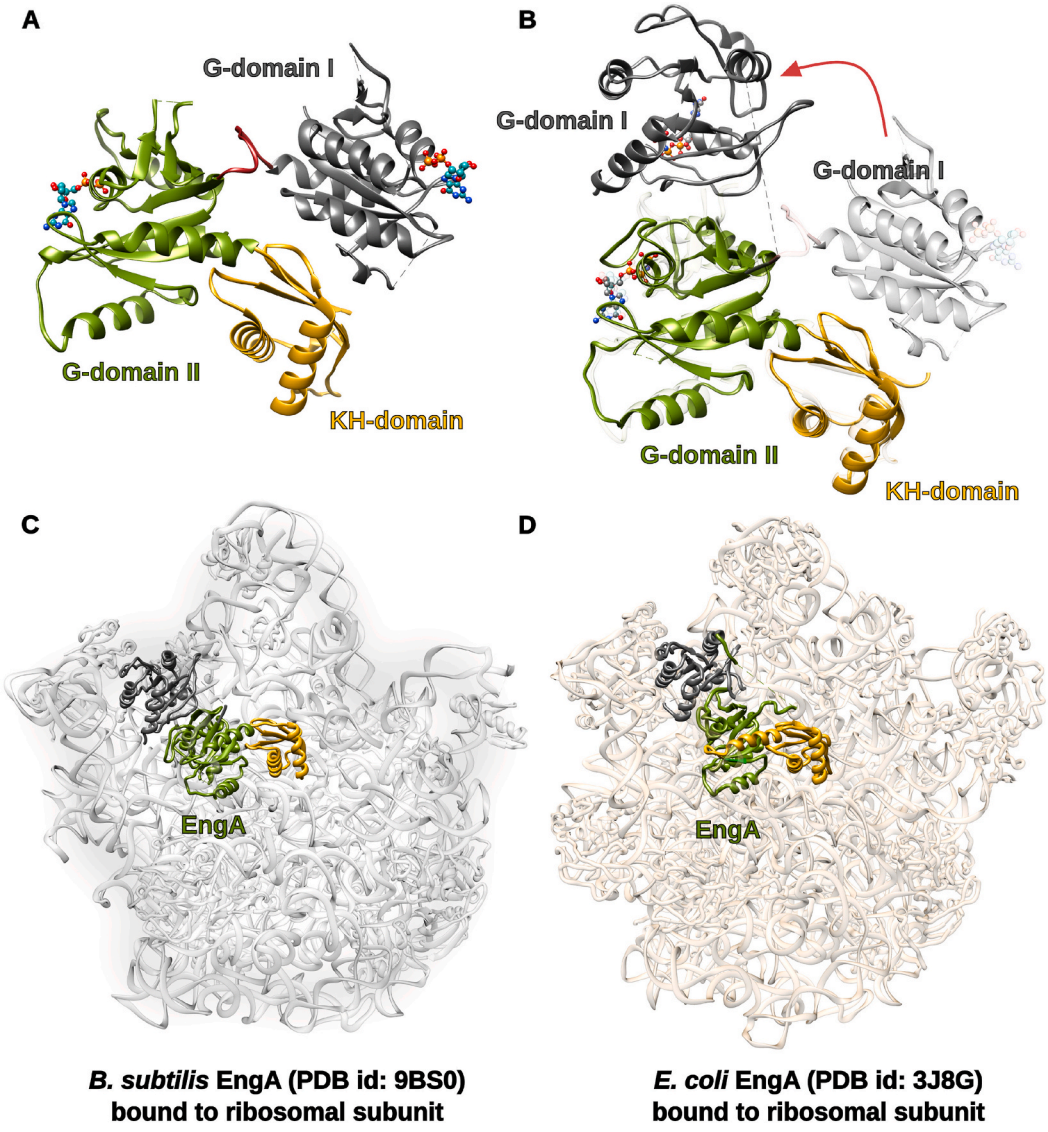

Fig. 2. (A) Crystal structure of GDP-bound *Bacillus subtilis* EngA (PDB ID: 4DCU). (B) Cryo-EM structure of GTP-analog (GMPPNP)-bound EngA extracted from the *B. subtilis* 45S ribosomal subunit-EngA complex (PDB ID: 9BS0). (C) Cryo-EM structure of the *B. subtilis* 45S ribosomal subunit with bound EngA. The GD1, GD2, and KH domains of EngA are highlighted in grey, green, and yellow, respectively. (D) Cryo-EM structure of the *Escherichia coli* 50S ribosomal subunit showing bound EngA, with GD1 in grey, GD2 in green, and the KH domain in yellow. (For interpretation of the references to colour in this figure legend, the reader is referred to the Web version of this article.)

of *C. burnetii* EngA in four different nucleotide-bound states: [GDP:GDP], [GDP:GTP-Mg^{2+}], [GTP-Mg^{2+}:GDP], and [GTP-Mg^{2+}:GTP-Mg^{2+}]. Here, [GDP:GDP] represents the state in which GDP is bound to both the GD1 and GD2 domains of CBEngA. In the [GDP:GTP-Mg^{2+}] bound state, GDP is bound to the GD1 domain, while GTP-Mg^{2+} is bound to the GD2 domain. In the [GTP-Mg^{2+}:GDP] bound state, GTP-Mg^{2+} is bound to the GD1 domain, and GDP is bound to the GD2 domain. The [GTP-Mg^{2+}:GTP-Mg^{2+}] state represents the system in which GTP-Mg^{2+} is bound to both the GD1 and GD2 domains.

2. Material and methods

2.1. Structure retrieval and MD simulations

Crystal structures of *Coxiella burnetii* EngA GTPases were obtained from the Protein Data Bank (PDB ID: 5DN8) [18,19]. Missing residues and atoms in these structures were modeled using Modeller 10.6 [20] through the UCSF Chimera 1.19 interface [21,22]. All the required CBEngA-nucleotide bound states [GDP:GDP], [GDP:GTP-Mg^{2+}], [GTP-Mg^{2+}:GDP] and [GTP-Mg^{2+}:GTP-Mg^{2+}] were prepared by aligning the required nucleotide onto the existing nucleotide of an available EngA-nucleotide complex in UCSF Chimera-1.19 [22]. The prepared models were validated by assessing hydrogen bond formation between the nucleotide and the conserved G-motifs of the G-domain.

All-atom molecular dynamics (MD) simulations, including both setup and production runs, were carried out using the GROMACS-24.3 [23–25] package, following the standard protocols cited in the literature [26,27]. Protein topologies were generated using the CHARMM36 [28–30] all-atom force field, while guanine nucleotide parameters were obtained from the CGenFF server [31–34]. Each EngA-nucleotide complex was placed inside a triclinic box with 1.2 nm spacing from the box edges. Further, the system was solvated with TIP3P model [35,36] water molecules. The system was neutralized by replacing the required number of solvent molecules with Cl^{-} ions. The [GDP:GDP] system was neutralized by adding 2 Cl^{-} ions, the [GDP:GTP-Mg^{2+}] system was neutralized by adding 3 Cl^{-} ions, the [GTP-Mg^{2+}:GDP] system was neutralized by adding 3 Cl^{-} ions, and the [GTP-Mg^{2+}:GTP-Mg^{2+}] system was neutralized by adding 4 Cl^{-} ions. Next, Energy minimization was

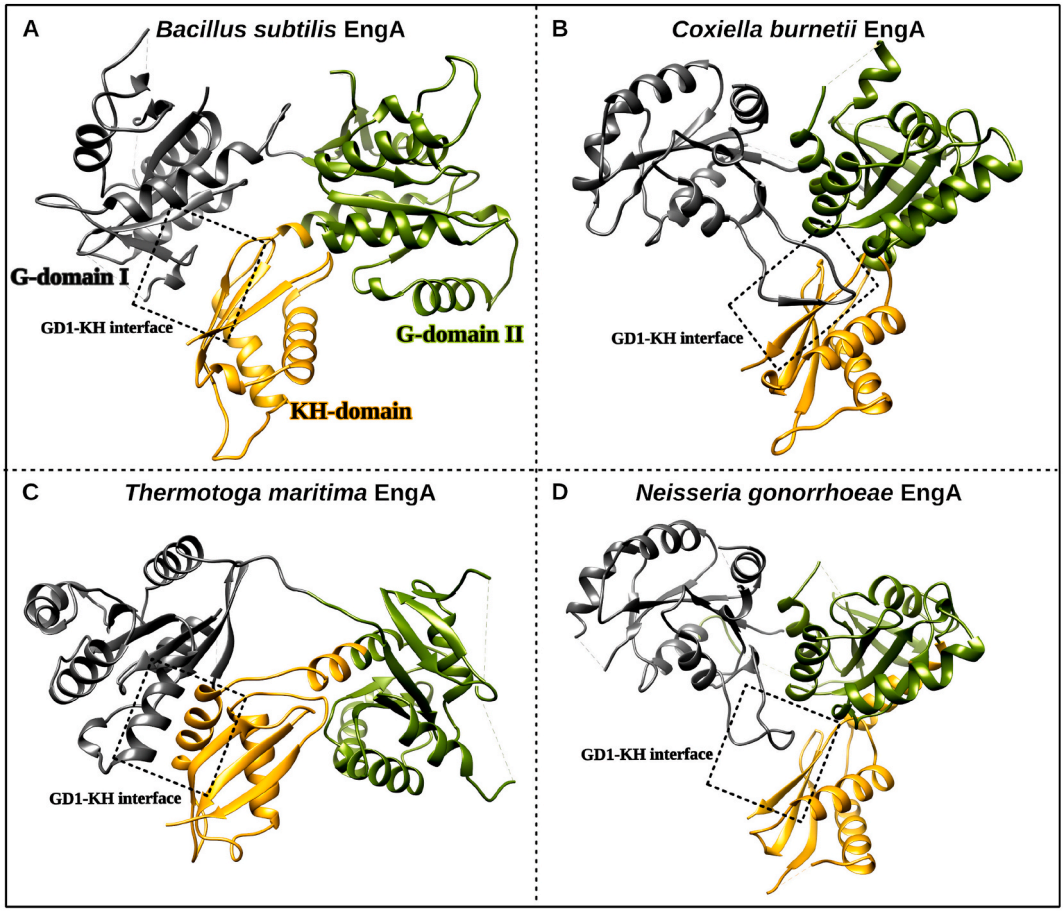

Fig. 3. Comparison of EngA crystal structures from different bacterial species. (A) *Bacillus subtilis* EngA (PDB ID: 4DCU). (B) *Coxiella burnetii* EngA (PDB ID: 5DN8). (C) *Thermotoga maritima* EngA (PDB ID: 1MKY). (D) *Neisseria gonorrhoeae* EngA (PDB ID: 6XRS). The boxed region highlights the GD1-KH interface in each structure.

performed using the steepest descent algorithm until the maximum force converged below 1000 kJmol^{-1}nm^{-1}, while also ensuring removal of steric clashes.

Subsequently, the system was first equilibrated in the NVT ensemble at 300 K temperature for 2 ns using the V-rescale thermostat [37], followed by equilibration in the NPT ensemble at 1 bar pressure and 300 K temperature for 2 ns using the Parrinello-Rahman barostat [38] and V-rescale thermostat, respectively. Finally, unrestrained production MD simulations were run for 1000 ns under NPT conditions. Long-range electrostatic interactions were computed with the Particle Mesh Ewald (PME) method [39,40], while all bond constraints involving hydrogen were maintained with the LINCS algorithm [41].

Further, to confirm the reliability of the nucleotide-dependent conformational changes, independent 1000 ns MD simulations were repeated for all the four bound systems i.e., [GDP:GDP], [GDP:GTP-Mg^{2+}], [GTP-Mg^{2+}:GDP] and [GTP-Mg^{2+}:GTP-Mg^{2+}]-bound EngA systems using identical MD protocols.

2.2. Preliminary analyses

Preliminary trajectory analyses, including root mean square deviation (RMSD) and root mean square fluctuations (RMSF), were performed using GROMACS 24.3 standard modules (gmx rms, gmx rmsf). Additional atomic distance measurements were performed using VMD-1.9.4 (Visual Molecular Dynamics) [42]. Distances between domain centers of mass (COMs) and angular measurements involving domain COMs were calculated using PLUMED-2.9.3 [43] software package. Structural and trajectory visualizations were generated using UCSF Chimera 1.19 and VMD-1.9.4. packages. Interactions between the GD1 and KH domains, such as hydrogen bonds, were evaluated through default plugins of VMD-1.9.4.

Interatomic contacts between the residues of the GD1-KH interface region for the EngA structures of *B. subtilis* (PDB ID: 4DCU), *C. burnetii* (PDB ID: 5DN8), *T. maritima* (PDB ID: 1MKY), and *N. gonorrhoeae* (PDB ID: 6XRS) were calculated using Arpeggio Webtool [44].

2.3. Interaction energy calculations

Interaction energy calculations were carried out to quantify the energetic contributions between important residues of EngA GTPases and bound nucleotides. For this purpose, the rerun option in GROMACS 24.3 was employed. A new binary run input file (.tpr) was generated using gmx grompp with the equilibrated structure, topology, and index files. The production trajectory (.xtc) was then processed using gmx mdrun -rerun, allowing recalculation of non-bonded interaction energies without modifying the original dynamics.

The Coulombic (electrostatic) and Lennard-Jones (van der Waals) interaction energies were extracted using the gmx energy module [45].

2.4. PCA analyses and porcupine plots

Principal component analysis (PCA) was employed to characterize the dominant collective motions of EngA during the MD trajectories. The covariance matrix of atomic positional fluctuations was constructed using Cα atoms after removal of overall translational and rotational motions [46,47]. The covariance matrix, C, was computed as:

$$C_{ij} = \langle (x_i - \langle x_i \rangle)(x_j - \langle x_j \rangle) \rangle$$

where x_i and x_j represent the coordinates of atoms i and j, respectively, and $\langle\cdot\rangle$ denotes the time average. Diagonalization of this matrix yielded eigenvalues and eigenvectors, with the first few eigenvectors (principal components) capturing the largest-amplitude motions of the protein [48]. PCA calculations were carried out using the GROMACS 24.3 tools (gmx covar, gmx anaeig).

To illustrate the motions specifically along first and second eigenvectors, porcupine plots were generated in VMD-1.9.4 using the PorcupinePlot.tcl script [42,49,50]. In these plots, arrows placed on Cα atoms indicate the direction and relative magnitude of displacements along the chosen eigenvector. Larger arrows represent higher-amplitude motions, allowing direct visualization of nucleotide-dependent domain rearrangements in EngA.

2.5. Construction of protein contact network and analyses

Protein contact networks (PCNs) were constructed from simulation frames using the Network View plugin of VMD-1.9.4 [51,52]. Each amino acid was represented by its Cα atom as a node, while the bound guanine nucleotide was represented by two nodes: (i) the N9 atom of the guanine base and (ii) the PB/PG atom of the terminal phosphate, representing the phosphate groups and ribose sugar. Edges were drawn between nodes (i) if nodes were not covalently bonded and (ii) whose residues are within a cutoff distance of 4.5 Å for at least 75 % of the total simulated trajectory [52].

Edge weights were determined from the cross-correlation between node motions, where the correlation between connected nodes, are computed as:

$$C_{ij} = \frac{\langle \Delta r_i . \Delta r_j \rangle}{\sqrt{\langle \Delta r_i . \Delta r_i \rangle \langle \Delta r_j . \Delta r_j \rangle}}$$

Here, $\langle\cdot\rangle$ represents the average, Δr represents $r - \langle r \rangle$, gives the displacement of a particular node i and j from its mean position. The complete set of values was assembled into dynamic cross-correlation map (DCCM) using Carma software [53].

The network was further partitioned into sub-networks (communities) using the Girvan-Newman algorithm [54], which iteratively removes edges with the highest betweenness (i.e., those most frequently traversed by shortest paths). The Floyd-Warshall algorithm [55]was then applied to compute the shortest paths between distant nodes, based on cumulative edge lengths:

$$d_{ij} = \sum_k w_{ik}$$

where d_{ij} is the shortest path length between nodes i and j, and w_{ik} is the weight of the edge connecting nodes i and k.

2.6. Secondary structure calculations

The secondary structure analysis was carried out using the Dictionary of Secondary Structure of Proteins (DSSP) algorithm [56]. For this, the timeline plugin of VMD-1.9.4 was employed to generate DSSP trajectories for all the simulated systems. The processed data were plotted and visualized as 2D heatmaps showing the time evolution of secondary structure elements (α-helix, β-strand, turn, and coil) of the key residues over the simulation time.

3. Results and discussion

3.1. Influence of nucleotide binding on EngA structural flexibility

The root mean square deviation (RMSD) of the Cα atoms was calculated over 1000 ns MD simulation trajectories to evaluate the conformational dynamics of EngA in different nucleotide-bound states: [GDP:GDP], [GDP:GTP-Mg^{2+}], [GTP-Mg^{2+}:GDP], and [GTP-Mg^{2+}:GTP-Mg^{2+}]. In all the simulated trajectories, the RMSD values remained within 0.5 nm relative to the starting structure (Fig. 4A), indicating the overall structural stability of EngA. However, the [GTP-Mg^{2+}:GDP] and [GTP-Mg^{2+}:GTP-Mg^{2}] bound states exhibited slightly higher deviations than the other bound states. To further evaluate the domain-specific deviation, the RMSD was analyzed separately for each domain of EngA (GD1, GD2, and KH). In the GD1 domain, the [GTP-Mg^{2+}:GTP-Mg^{2+}] state showed a slightly higher deviation (Fig. 4B), whereas in the GD2 domain, the [GTP-Mg^{2+}:GDP] state displayed comparatively higher deviations (Fig. 4C). The KH domain remained stable in all nucleotide-bound states (Fig. 4D).

Further residue-wise fluctuations were evaluated using RMSF analysis (Fig. S3). The results showed that the loop regions and C-terminal tail exhibited the greatest fluctuations, and C-tail fluctuations were due to their unrestrained and flexible structure. Among the loop regions, SwI and SwII of GD1, the linker, and SwI and SwII of GD2 exhibited the highest fluctuation. In particular, SwI (residue number: 23–41) and SwII (residue number: 56–73) of GD1 showed distinguished differences in fluctuations between systems, with higher flexibility observed in the [GTP-Mg^{2+}:GDP] and [GTP-Mg^{2+}:GTP-Mg^{2+}] states than in the [GDP:GDP] and [GDP:GTP-Mg^{2+}] states. To further evaluate these differences, the RMSD was calculated for the SwI and SwII regions of GD1 over the simulation time (Fig. 5). In the SwI region, conformational transitions occurred in both [GTP-Mg^{2+}:GDP] and [GTP-Mg^{2+}:GTP-Mg^{2+}] states, with greater deviation observed in the [GTP-Mg^{2+}:GTP-Mg^{2+}] system (Fig. 5A). Similarly, the SwII region displayed slightly higher deviations in the [GTP-Mg^{2+}:GDP] and [GTP-Mg^{2+}:GTP-Mg^{2+}] states compared to the [GDP:GDP] and [GDP:GTP-Mg^{2+}] states (Fig. 5B). These results highlight that the presence of GTP-Mg^{2+} in GD1 induces distinct conformational behavior compared to GDP-bound GD1.

Furthermore, to extract the essential motions from the trajectory, principal component analysis (PCA) was performed along the first and second eigenvectors. Porcupine plots were used to visualize these motions, where the arrow direction indicates the direction of movement, and the arrow length represents the amplitude of movement. Porcupine plot analysis along the first eigenvector revealed distinct dynamics across nucleotide-bound states (Fig. 6). In the [GDP:GDP] state, the GD1 exhibited major motions directed toward the KH domain, with the KH domain showing directed motion toward GD1 (Fig. 6A). In the [GDP:GTP-Mg^{2+}] state, the dominant displacement was localized to SwII of GD1, along with KH domain motion towards GD1 (Fig. 6B). In the [GTP-Mg^{2+}:GDP] state, significant displacement was observed in SwI of GD1 (Fig. 6C), whereas in the [GTP-Mg^{2+}:GTP-Mg^{2+}] state (Fig. 6D), SwII of GD1 exhibited prominent motion directed toward SwI of GD1. Furthermore, the porcupine plot along the second eigenvector revealed distinct patterns of motion (Fig. 7). In the [GDP:GDP] bound state, the KH domain shifted toward the GD1 domain with a greater magnitude than that observed along the first eigenvector (Fig. 7A). The [GDP:GTP-Mg^{2+}] state showed dominant motion in SwII of GD1, as observed along the first eigenvector (Fig. 7B). In the [GTP-Mg^{2+}:GDP] state, SwII of GD2 shifted toward SwI of GD1, resembling the motion observed in the [GTP-Mg^{2+}:GTP-Mg^{2+}] state along the first eigenvector (Fig. 7C). Interestingly, in the [GTP-Mg^{2+}:GTP-Mg^{2+}] state, GD1 and the KH domain moved away from each other, indicating large-scale conformational changes (Fig. 7D).

Overall, this analysis provides insights into the nucleotide-dependent dynamics of EngA. In the [GDP:GDP] bound state, the GD1 domain approaches the KH domain, whereas in the [GTP-Mg^{2+}:GTP-Mg^{2+}] bound state, the GD1 and KH domains move away from each other. Additionally, SwII of GD1 movements were seen approaching SwI of GD1 in the [GTP-Mg^{2+}:GDP] and [GTP-Mg^{2+}:GTP-Mg^{2+}] systems, consistent with the higher RMSD deviations observed for SwII in these two systems.

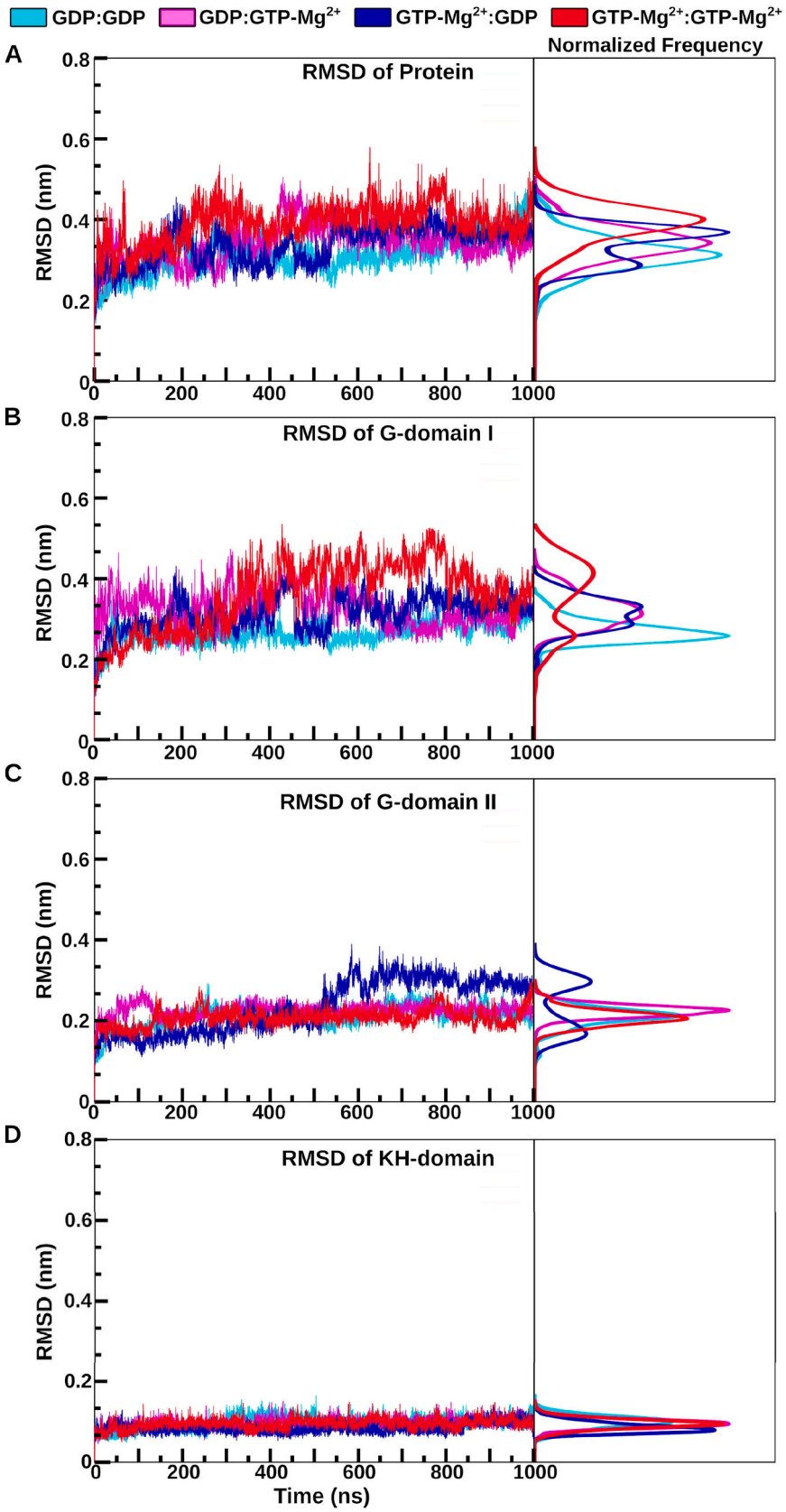

Fig. 4. (A–D) The root mean square deviation plot of Cα atoms of *Coxiella burnetii* EngA with respect to the NPT equilibrated structure.

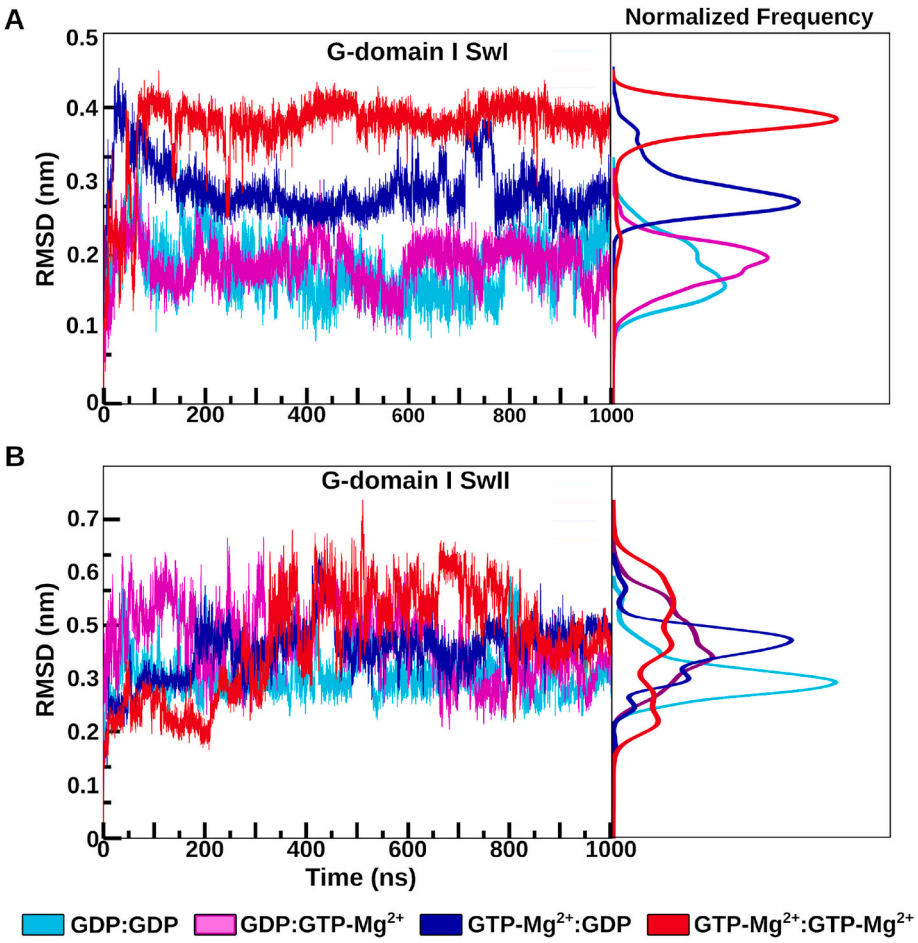

Fig. 5. Root mean square deviation plots of *Coxiella burnetii* EngA with respect to the NPT equilibrated structure: (A) Cα atoms of SwI residues (residues 23–41) of GD1 and (B) Cα atoms of SwII residues (residues 56–73) of GD1.

3.2. Nucleotide-dependent GD1-KH interface interactions and domain motion

Porcupine plot analysis provided insight into the essential motions of EngA, which are dominated by nucleotide-dependent GD1 and KH domain movements. To quantify the effect of these essential motions on domain interactions, hydrogen bonds, and non-bonded interaction energies at the GD1-KH interface were analyzed for all simulated trajectories (Fig. 8). Hydrogen bond analysis showed that in the [GDP:GDP] and [GDP:GTP-Mg^{2+}] states, a maximum of four and five hydrogen bonds, respectively, were formed at the GD1-KH interface (Fig. 8B). The primary interactions involved Val30 (donor)-Ile428 (acceptor), Val30 (acceptor)-Ile428 (donor), and Leu430 (donor)-Ala28 (acceptor). In the [GTP-Mg^{2+}:GDP] state, up to three hydrogen bonds were consistently observed between the same residues. In contrast, the [GTP-Mg^{2+}:GTP-Mg^{2+}] bound state showed disruption of the interface H-bonds within the first 25 ns (Fig. 8B). Furthermore, the nonbonded interaction energies (Coulombic and van der Waals energies) were consistent with the hydrogen bond analysis. The [GDP:GDP] and [GDP:GTP-Mg^{2+}] states maintained the strongest GD1-KH interactions, with average energies of −175 kJ/mol throughout the simulation. In the [GTP-Mg^{2+}:GDP] complex, the interaction energy decreased to −130 kJ/mol, whereas the [GTP-Mg^{2+}:GTP-Mg^{2+}] bound state exhibited the weakest interactions, indicating disruption of the GD1-KH interface (Fig. 8A).

The changes observed in GD1-KH interactions prompted an investigation of the secondary structural variations at the interface (Fig. 8C, S4, and S5). In the [GDP:GDP] and [GDP:GTP-Mg^{2+}] states, the β-strand spanning residues 29–32 at the GD1 interface remained stable throughout the simulation (Fig. S5A and S5B). In the [GTP-Mg^{2+}:GDP] state, this β-strand is shortened to residues 29–30 (Fig. S5C), while in the [GTP-Mg^{2+}:GTP-Mg^{2+}] state, residues 29–32 are unwind from β-strand to coil, turn, and β-bridge within the first nanosecond (Fig. S5D). The weakening of GD1-KH interactions in [GTP-Mg^{2+}:GTP-Mg^{2+}] is associated with the structural transition of the β-strand. The [GTP-Mg^{2+}:GDP] system also exhibited reduced interaction energy along with secondary structural changes, whereas [GDP:GDP] and [GDP:GTP-Mg^{2+}] retained stable β-strands and stronger interface contacts.

These observations suggest that nucleotide binding induces structural alterations at the GD1 interface, which influence its interaction with the KH domain. Consistent with our findings, experimental studies have demonstrated that disruption of the GD1-KH interface is essential for EngA association with the 50S ribosomal subunit [9,12]. This association occurs in the [GTP:GTP] bound state, representing the active "on state." In support to this cryo-electron microscopy structures of ribosome-bound *E. coli* and *B. subtilis* EngA in a GTP-analogue (GMPPNP) bound state show that GD1 is away from KH domain, leaving the interface open to associate with the 50S ribosomal subunit (Fig. 2B). In contrast, the crystal structures of *B. subtilis* and *C. burnetii* EngA in GDP-bound states reveal a closed GD1-KH interface (Fig. 3A and B), corresponding to the inactive "off state". In agreement with this, our study also revealed the disruption of the GD1-KH interface in the [GTP-Mg^{2+}:GTP-Mg^{2+}] bound state. The GD1-KH interface is more strongly associated in the [GDP:GDP] bound state.

To examine how disruption or retention of the GD1-KH interface in our simulations influences GD1 domain motion, we compared the simulated trajectories with experimental closed and open state

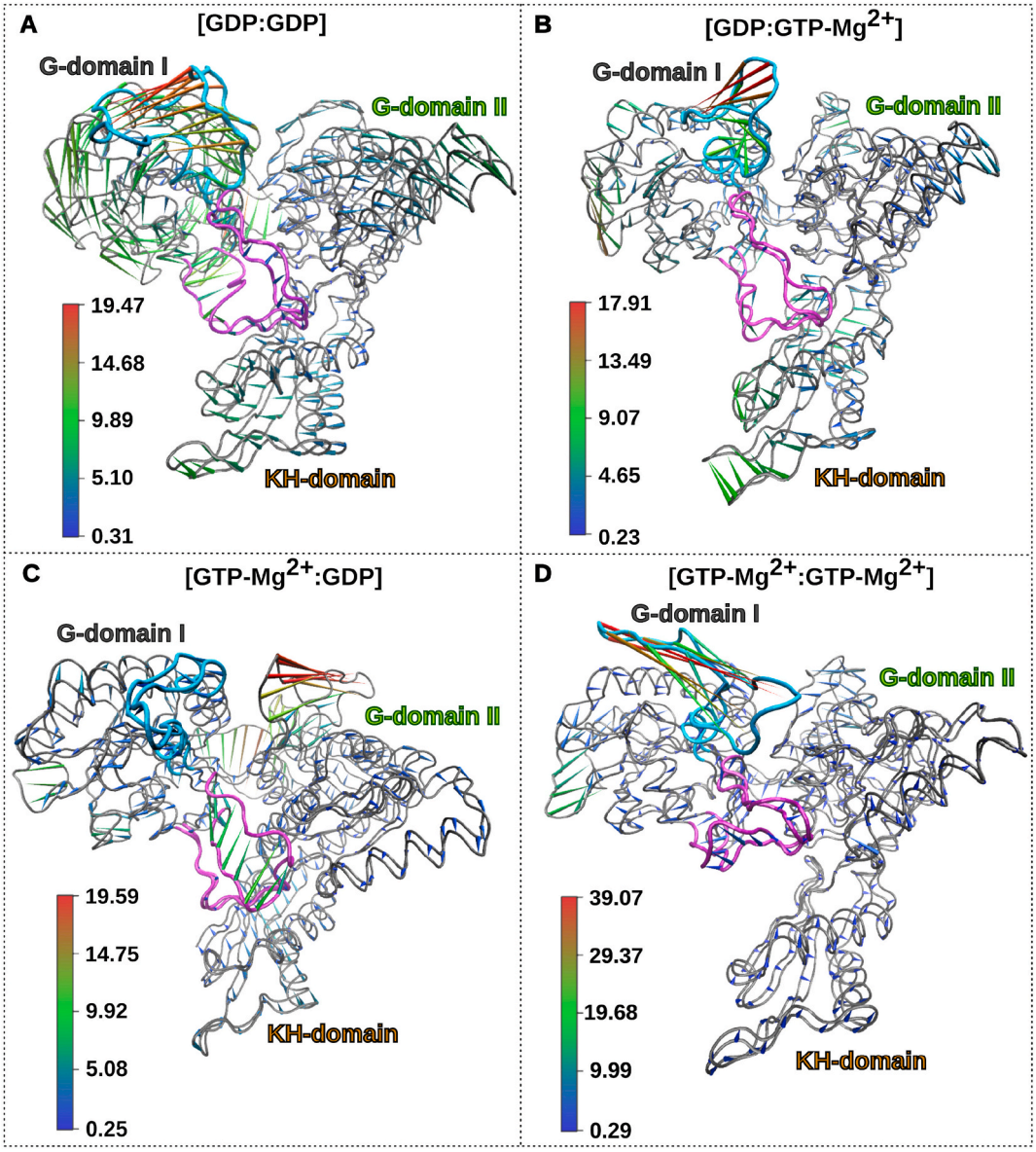

Fig. 6. (A–D) Porcupine plots representing the dominant motions of ***Coxiella burnetii*** EngA in different nucleotide-bound states, generated from the extreme structures along the first principal component.

structures. For this quantitative comparison, we measured two collective variables: the distance between center of mass (COM) of GD1 and KH and the angle formed by COM of KH, GD1, and GD2 domains respectively. This angle was chosen because it provides a clear distinction between closed crystal structures (PDB: 4DCU) and open ribosome-bound electron microscopy structures (PDB: 9BS0). In the crystal structure of the [GDP:GDP] bound (off) state, the center-of-mass (COM) distance between GD1 and the KH domain is 4.01 nm, and the angle formed by the COMs of KH, GD1, and GD2 is 50° (Fig. 9A). In the ribosome-associated EngA observed in the electron microscope structure ("on" state), the GD1-KH COM distance is 5.67 nm, while the COM angle between KH, GD1, and GD2 is 29° (Fig. 9B). To determine whether similar domain motions occurred in our simulations, scatter plots of these two variables, distance and angle, were generated for all trajectories (Fig. 9C). The plots show that the [GDP:GDP] system maintained a short GD1-KH distance, decreasing to 3.54 nm, with the KH-GD1-GD2 angle reaching 54°, resembling the closed crystal structure (Fig. 9A and D). In contrast, the [GTP-Mg^{2+}:GTP-Mg^{2+}] system exhibited an increased GD1-KH distance of up to 5.13 nm and a reduced angle of 41°, resembling the electron microscopy structure (Fig. 9B and E). These observations indicate that disruption of the GD1-KH interface in the [GTP-Mg^{2+}:GTP-Mg^{2+}] system displaces GD1 from KH, in agreement with the domain motions observed in the ribosome-bound EngA open state.

Furthermore, the [GDP:GTP-Mg^{2+}] and [GTP-Mg^{2+}:GDP] bound states exhibit dynamics similar to the [GDP:GDP] and [GTP-Mg^{2+}:GTP-Mg^{2+}] systems, respectively, highlighting the role of GTP-Mg^{2+} in GD1 in promoting disruption of the GD1-KH interface. In the [GTP-Mg^{2+}:GDP] bound state, the interaction energy between GD1 and KH decreased compared to that in the [GDP:GDP] and [GDP:GTP-Mg^{2+}] systems, accompanied by secondary structural changes. Although the GD1-KH domain distance remains comparable to those in the [GDP:GDP] and [GDP:GTP-Mg^{2+}] bound states, the KH-GD1-GD2 angle in the [GTP-Mg^{2+}:GDP] bound state decreases, similar to that in the [GTP-Mg^{2+}:GTP-Mg^{2+}] bound state. In contrast, in the [GDP:GTP-Mg^{2+}] system, the GD1-KH interaction energy is stable, similar to the [GDP:GDP] bound state, and the KH-GD1-GD2 angle also resembles the [GDP:GDP] bound state. These observations suggest that the presence of GTP-

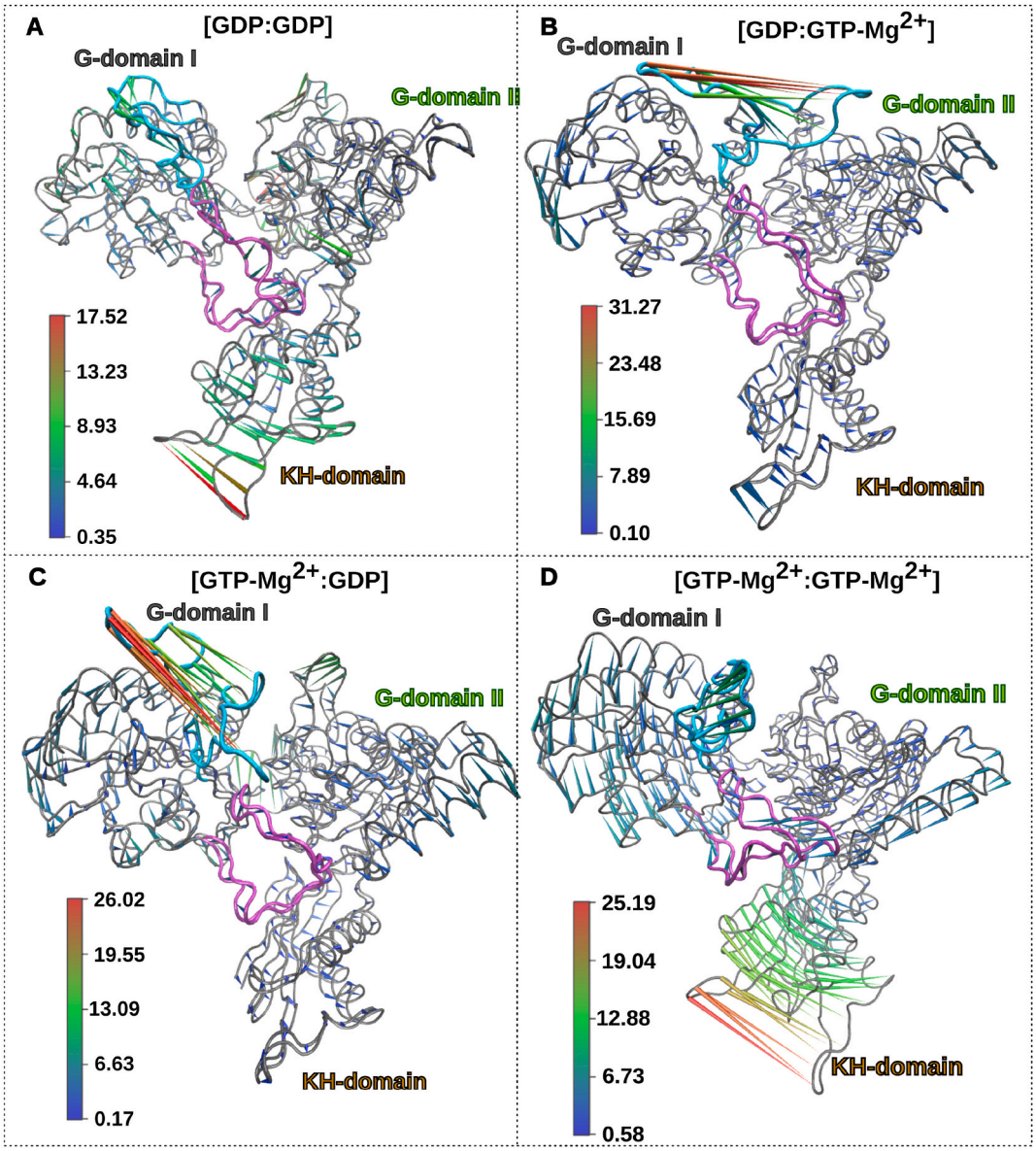

Fig. 7. (A–D) Porcupine plots representing the dominant motions of *Coxiella burnetii* EngA in different nucleotide-bound states, generated from the extreme structures along the second principal component.

Mg^{2+} in GD1 may be responsible for the disruption of the GD1-KH interface and the associated domain motions. Overall, this study demonstrates that nucleotide binding strongly influences the motion of the EngA domains. In the [GTP-Mg^{2+}:GTP-Mg^{2+}] bound state, disruption of the GD1-KH interface displaces GD1 away from KH, facilitating the EngA-ribosome association. In contrast, in the [GDP:GDP] and [GDP:GTP-Mg^{2+}] bound states, the GD1-KH interface remains intact, maintaining a close association between the GD1 and KH domains.

3.3. Network connectivity and Arg40 interactions modulating GD1-KH dynamics

While conformational analysis has highlighted nucleotide-driven domain motions, the underlying molecular mechanisms by which these nucleotides induce such changes need to be addressed. To gain this insight, community network analysis was performed, which maps the communication pathways within the protein and identifies how local nucleotide interactions propagate through the domains. Community network analysis revealed differences in connectivity across nucleotide states, with 15 communities identified for the [GDP:GDP] state, 13 for the [GDP:GTP-Mg^{2+}] state, 11 for the [GTP-Mg^{2+}:GDP] state, and 13 for the [GTP-Mg^{2+}:GTP-Mg^{2+}] state (Fig. S6). Analysis of specific community extensions shows that the [GDP:GDP] and [GDP:GTP-Mg^{2+}] states exhibit network connections extending from the nucleotide-binding pocket to the GD1 SwI region, followed by connectivity between GD1 interface (GD1 SwI) and the KH domain (Fig. 10A and B). In the [GTP-Mg^{2+}:GDP] state, the extension from the nucleotide-binding site to SwI was reduced (Fig. 10C), whereas the GD1 interface-KH connection remained present but was less prominent than in the [GDP:GDP] and [GDP:GTP-Mg^{2+}] states. In contrast, the [GTP-Mg^{2+}:GTP-Mg^{2+}] state lacked community extension from the nucleotide-binding site to SwI and exhibited no connectivity between the GD1 interface (GD1 SwI) and KH domains, indicating a complete disruption of the inter-domain network (Fig. 10D). Interestingly, a community extension was observed between the GD1 SwI region and GD2 (Fig. 10D). This GD1-GD2 connectivity is also present in the [GTP-Mg^{2+}:GDP] state (Fig. 10C) but is absent in the [GDP:GDP] and [GDP:GTP-Mg^{2+}] states (Fig. 10A and B).

Overall, this analysis highlights the influence of nucleotides on the

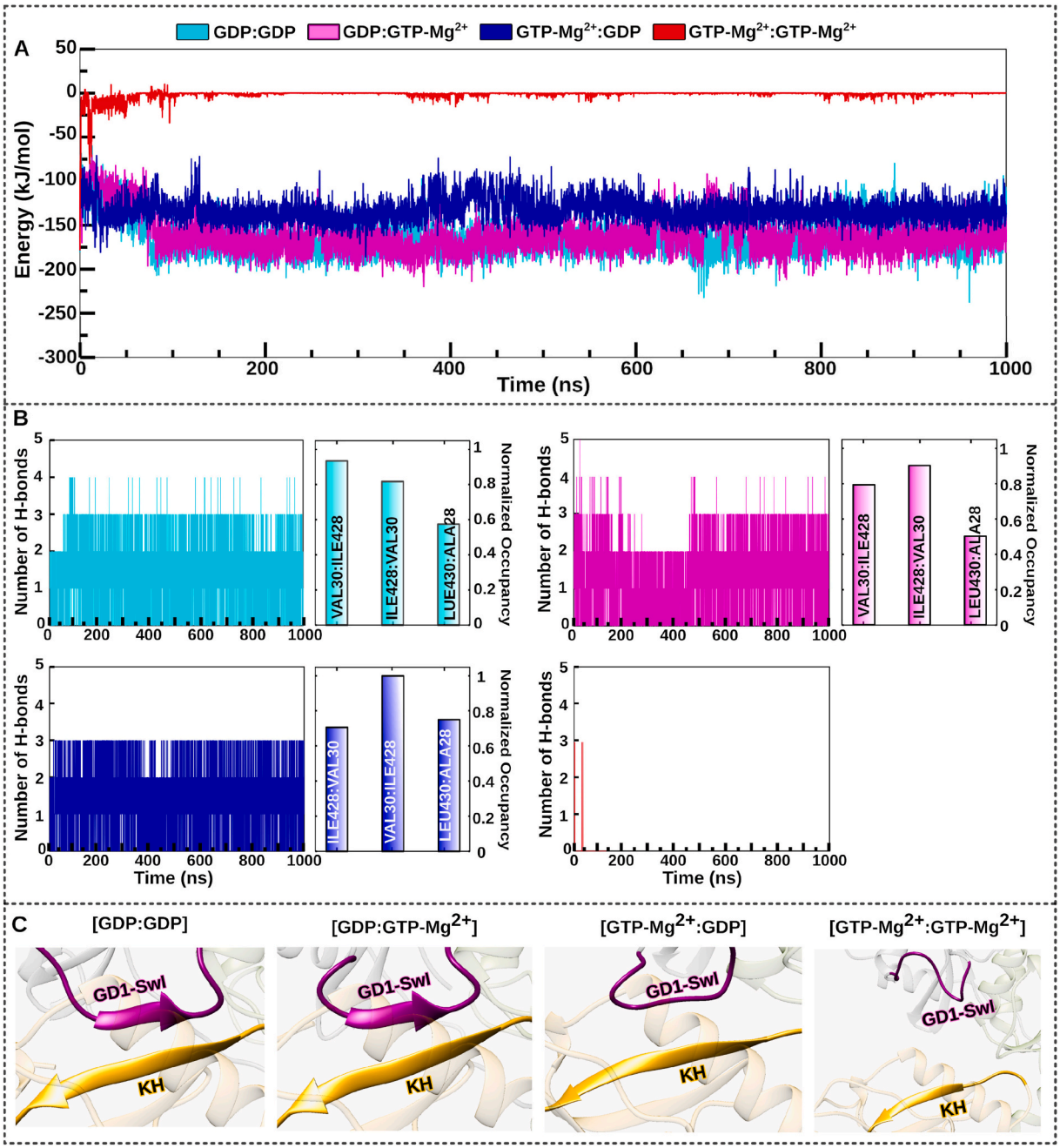

Fig. 8. (A) Interaction energy (Coulombic and van der Waals) between the GD1 interface (residues 28–33) and KH interface (residues 425–430). (B) Hydrogen bond analysis between the GD1 interface (residues 28–33) and KH interface (residues 425–430). (C) Visual representation of the GD1-KH interface at 990 ns across all simulated systems.

intrinsic connectivity within EngA. In the [GDP:GDP] and [GDP:GTP-Mg^{2+}] states, nucleotide-driven communication stabilizes the GD1 SwI region and strengthens its interaction with the KH domain, thereby maintaining a closed conformation. In contrast, in the [GTP-Mg^{2+}:GTP-Mg^{2+}] state, no extended network from GTP to GD1-SwI was observed, leaving SwI unrestrained and weakening its interaction with KH domain. This disruption of the GD1 SwI-KH interface enables GD1 SwI to establish new connectivity with GD2, driving GD1 toward the open conformation required for EngA association with the 50S ribosomal subunit.

The influence of the nucleotide on SwI community extension was revealed through distance calculations between the nucleotide and SwI residue (Fig. 11). In the [GDP:GDP] bound state, the negatively charged terminal phosphate of GDP is attracted to the positively charged Arg40 residue of SwI. This interaction was confirmed by distance calculations between Arg40 (CZ) and the terminal phosphate (GDP:PB/GTP:PG). This interaction anchors SwI to the nucleotide, thereby stabilizing SwI and preventing disruption of the GD1 SwI interaction with the KH domain. In contrast, in the [GTP-Mg^{2+}:GTP-Mg^{2+}] and [GTP-Mg^{2+}:GDP] states, the presence of positively charged Mg^{2+} prevents the positive charge of Arg40 from being attracted to the nucleotide. Consequently, the nucleotide no longer anchors SwI, leading to SwI destabilization and potentially weakening its interaction with the KH domain. Interestingly, in the [GTP-Mg^{2+}:GDP] and [GTP-Mg^{2+}:GTP-Mg^{2+}] states, Arg40 of GD1 SwI appears to form alternative interactions with the SwII region of GD1. This is supported by PCA porcupine analysis (Figs. 6 and 7), which highlights the key motion in which SwII moves toward SwI in these nucleotide-bound states.

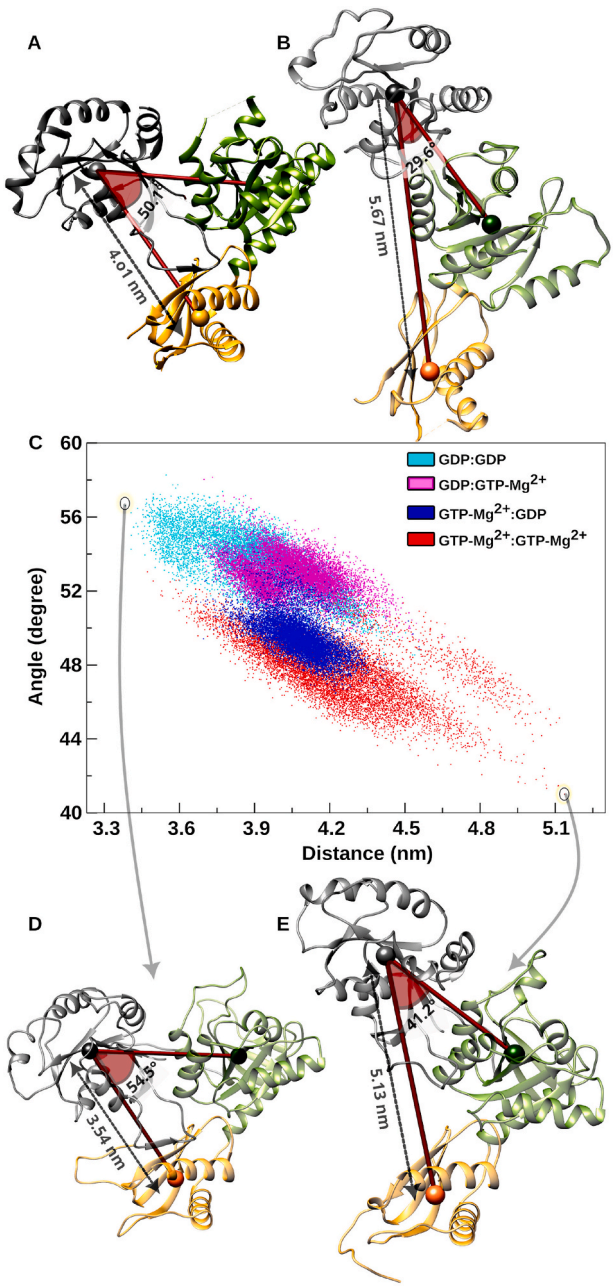

Fig. 9. Structural and conformational analysis of EngA: (A) Crystal structure of *C. burnetii* EngA (PDB ID: 5DN8). (B) Cryo-EM structure of EngA extracted from the 45S subunit-EngA complex (PDB ID: 9BS0). (C) Scatter plot of the distance between GD1 and KH domains versus the angle formed by KH, GD1, and GD2. (D) Structures extracted from the scatter plot corresponding to the lowest GD1-KH distance ([GDP:GDP] bound state). (E) Structures extracted from the scatter plot corresponding to the maximum GD1-KH distance ([GTP-Mg^{2+}:GTP-Mg^{2+}] bound state). The calculated GD1-KH distances and KH-GD1-GD2 angles for all depicted structures are indicated.

To further validate this mechanism, the interaction energy between Arg40 of SwI and the SwII region of GD1 was calculated for all simulated systems (Fig. S7). In the [GTP-Mg^{2+}:GTP-Mg^{2+}] bound state, the nonbonded interaction energy between Arg40 and SwII reached a maximum of −175 kJ/mol (Fig. S7D), whereas in the other systems, no persistent interactions were observed (Figs. S7A, S7B, and S7C).

This study shows that the presence of Mg^{2+} with the GTP plays a key role in regulating the transition between the open and closed conformations of CBEngA. As we see in the [GTP-Mg^{2+}:GTP-Mg^{2+}] bound state, Mg^{2+} at the nucleotide binding site prevents the positively charged Arg40 of the Switch I (SwI) region from interacting with the nucleotide (Fig. 11). As a result, the GD1 SwI region becomes unstable, this inturn weakens GD1 SwI interaction with KH domain. This destabilization allows the GD1 and KH domains to move apart, leading to an open conformation (Fig. 9C and E). By understanding the importance of Mg^{2+} along with GTP in attaining the open conformation of EngA, we simulated the [GTP:GTP] state without Mg^{2+} to analyse the EngA dynamics in the Mg^{2+} absence. Interestingly, in the [GTP:GTP] bound state, the GD1-KH interface remained stable, and the GD1 and KH domains did not move away from each other (Fig. S8). Community network analysis showed that in the [GTP:GTP] bound state, the communication extends from the nucleotide to the SwI region and also community extension is seen between the GD1 and KH domain interface (Fig. S9). Further, the influence of the nucleotide in the [GTP:GTP] state is analyzed through distance calculation, which revealed an interaction between the negatively charged terminal phosphate of GTP and the positively charged Arg40 of Sw I (Fig. S10). This nucleotide-driven communication stabilizes SwI and strengthens the GD1-KH interaction, keeping the CBEngA in a closed conformation. Overall, these results show that the presence of Mg^{2+} is crucial for CBEngA to adopt the open conformation. This is in agreement with previous studies on GTPases that emphasize the role of Mg^{2+} in enabling GTPases to attain the active conformation [13,57].

This study emphasize how different nucleotides influence the intricate network of interactions within EngA, modulating its functional "off" and "on" states. In the [GDP:GDP] and [GDP:GTP-Mg^{2+}] bound states, Arg40 interacts with the negatively charged terminal phosphate of GDP. This interaction stabilizes SwI, allowing it to maintain contact with the KH domain through extended community connectivity, thereby supporting the closed conformation. In contrast, in the [GTP-Mg^{2+}:GTP-Mg^{2+}] bound state, the presence of positively charged Mg^{2+} prevents Arg40 from interacting with the nucleotide. Instead, Arg40 was drawn toward the negatively charged residues in the GD1 SwII region. This alternative interaction effectively pulls SwI away from KH, weakening the SwI-KH interface interactions and facilitating community extension between GD1 SwI (GD1 interface) and GD2. A similar behavior was observed in the [GTP-Mg^{2+}:GDP] state, where, although direct Arg40-SwII interactions were weaker, community extensions toward GD2 and reduced GD1-KH stability were observed.

These results suggest that the presence of [GTP-Mg^{2+}] in GD1 is essential for disrupting the GD1-KH interface and allowing GD1 to adopt an open conformation that facilitates EngA binding to the 50S ribosomal subunit. This study emphasizes that, similar to *B. subtilis* EngA, *C. burnetii* EngA also undergoes disruption of the GD1-KH interface in its GTP-bound state. This pattern of interface disruption is primarily influenced by the charge state of nucleotide.

To validate the reliability of the observed global motions, the simulations were replicated. The results of the replicated simulations were consistent with the initial set, confirming nucleotide-dependent conformational changes (Figs. S11, S12, S13, and S14).

4. Conclusion

In this study, 1000 ns molecular dynamics simulations of *Coxiella burnetii* EngA were performed in four nucleotide-bound states ([GDP:GDP], [GDP:GTP-Mg^{2+}], [GTP-Mg^{2+}:GDP], and [GTP-Mg^{2+}:GTP-Mg^{2+}]) to understand the nucleotide-dependent conformational dynamics and interdomain communication. RMSD, RMSF, and PCA analyses revealed nucleotide-dependent dynamic behavior of the GD1 and KH domains. In the [GTP-Mg^{2+}:GTP-Mg^{2+}] state, the GD1 and KH domains moved apart, whereas in the [GDP:GDP] state, they approached each other, representing open and closed conformations, respectively, consistent with electron microscopy and crystal structure. Furthermore, interaction energy and H-bond calculations between the GD1-KH interface showed that in the [GTP-Mg^{2+}:GTP-Mg^{2+}] state, GD1-KH

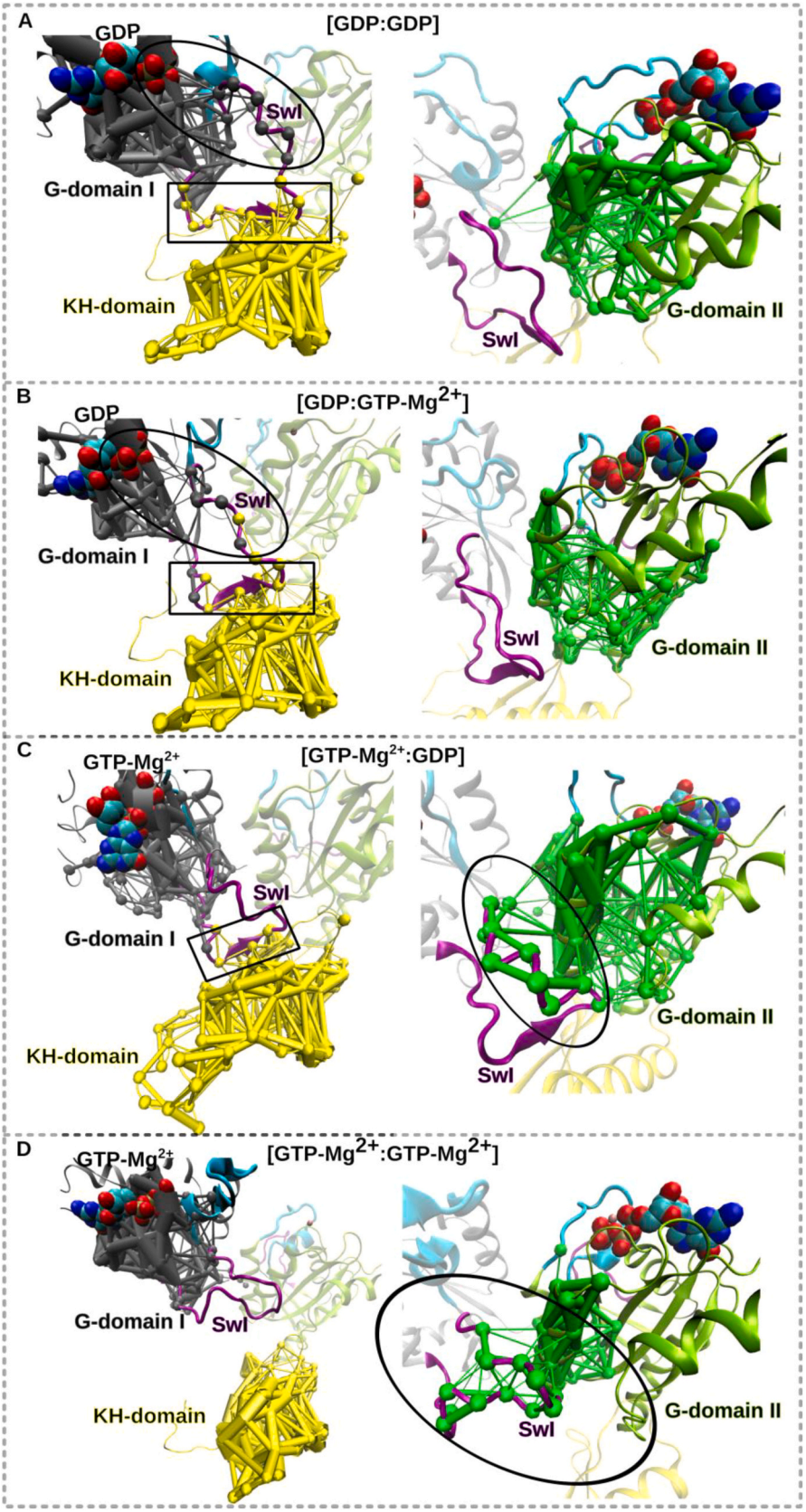

Fig. 10. Communities of the protein contact networks (PCNs). (A and B) Extended community from the nucleotide-bound state to SwI (ellipse), followed by community extension from SwI to the KH domain (box). (C and D) No community extension from the nucleotide-bound state to SwI, but extended community observed between GD1 SwI and GD2 (ellipse).

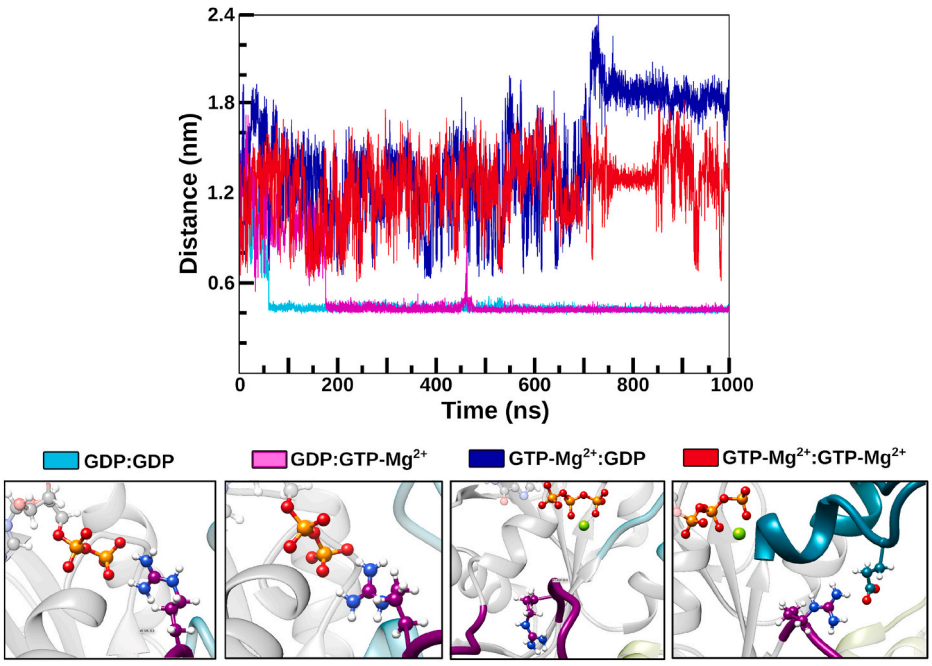

Fig. 11. Distance between the terminal phosphates of the nucleotide (GDP:PB/GTP:PG) and Arg40 (CZ). The visual depiction of the corresponding bound states, with Arg40 in violet, terminal phosphates in orange, and Mg^{2+} in green. (For interpretation of the references to colour in this figure legend, the reader is referred to the Web version of this article.)

interface interactions were disrupted within the first 10 ns, whereas in the [GDP:GDP] and [GDP:GTP-Mg^{2+}] states, these interactions remained stable. Additionally, the scatter plot of the distance between the GD1 and KH domains and angle formed by KH-GD1-GD2 further indicated that EngA alternates between "on" and "off" states corresponding to [GTP-Mg^{2+}:GTP-Mg^{2+}] and [GDP:GDP], respectively. The open (on) conformation results from the GD1-KH disruption and the movement of GD1 away from KH, aligning with structural observations in *B. subtilis* EngA.

Furthermore, community network analysis revealed the molecular basis of this communication, in which GDP bound to GD1 leads to extended connectivity from the nucleotide to the SwI region of GD1, thereby stabilizing SwI-KH interactions and restricting GD1 movement. In contrast, GTP-Mg^{2+} lacks this connectivity, causing a loss of communication between the nucleotide and SwI, which destabilizes the SwI-KH interactions. This allows SwI to form an alternative community with GD2, leading to GD1-KH disruption and promoting the open conformation in the [GTP-Mg^{2+}:GTP-Mg^{2+}] state. Furthermore, the distance between the terminal phosphate of the bound nucleotide and Arg40 of SwI highlights the importance of the charge state of the bound nucleotide in driving these conformational changes. When GDP is bound to GD1, its negatively charged phosphate groups attract the positively charged Arg40 of SwI, as shown by distance analysis. This interaction facilitates the extension of the community between the nucleotide and SwI by stabilizing the GD1-KH interface. Conversely, when GTP-Mg^{2+} is bound, the presence of positive Mg^{2+} prevents the positively charged Arg40 from engaging with the nucleotide. This leaves SwI free to interact with GD2, leading to GD1-KH interface disruption and conformational rearrangement.

Overall, this study provides detailed mechanistic insights into how nucleotide charge states govern internal connectivity and conformational transitions in *C. burnetii* EngA. The results demonstrate that the GTP-bound state promotes GD1-KH disruption and domain separation, whereas the GDP-bound state stabilizes the closed conformation via charge-mediated connectivity. Importantly, despite the differences in the crystal structures of *B. subtilis* and *C. burnetii* EngA in their GDP-bound forms, both retain GD1-KH interface interactions and exhibit a similar nucleotide-dependent switching mechanism. These findings not only elucidate the molecular basis of the EngA on/off switching mechanism but also highlight its potential as a therapeutic target. Since EngA is essential for bacterial ribosome biogenesis and lacks any human orthologs, identifying small molecules that can stabilize its "off" (GDP-like) state or prevent GD1-KH disruption could inhibit ribosome assembly and, consequently, bacterial protein synthesis. This approach could serve as a promising strategy for developing novel antibacterial compounds against *C. burnetii* and other pathogenic bacteria.

CRediT authorship contribution statement

K.M. Kavya: Writing – review & editing, Writing – original draft, Visualization, Validation, Methodology, Investigation, Formal analysis, Data curation, Conceptualization. **Guruswaroop C:** Writing – review & editing, Visualization, Methodology, Formal analysis, Data curation. **Upendra N:** Software, Methodology, Data curation, Conceptualization. **Krishnaveni S:** Writing – review & editing, Validation, Supervision, Resources, Project administration, Funding acquisition, Conceptualization.

Disclosure statement

No potential conflict of interest was reported by the authors.

AI assistance declaration

The authors declare that artificial intelligence (AI) tool ChatGPT was used for language refinement. No part of the data analysis, interpretation, or scientific content was generated by AI. All scientific conclusions and results were formulated by the authors.

Acknowledgment

This work was supported by the Department of Science and Technology (DST), Government of India, under the SERB-SURE project grant (Project No. SUR/2022/005410), for which the authors express their

sincere gratitude. Authors thank the University of Mysore for providing the necessary facilities to carry out this research. Kavya K. M. acknowledges the Department of Science and Technology (DST), Government of Karnataka, for financial support through the Karnataka DST-Ph.D. Fellowship. The authors wish to express their profound appreciation to the Rashtriya Uchchatar Shiksha Abhiyan (RUSA 2.0) program of the Government of India for its funding of infrastructure and research activities under Research Innovation and Quality Improvement (Component-10), which is being implemented through the University of Mysore.

Appendix A. Supplementary data

Supplementary data to this article can be found online at https://doi.org/10.1016/j.abb.2025.110693.

Data availability

Data will be made available on request.

References

[1] H.R. Bourne, D.A. Sanders, F. McCormick, The GTPase superfamily: a conserved switch for diverse cell functions, Nature 348 (1990) 125–132.
[2] K. Karbstein, Role of GTPases in ribosome assembly, Biopolymers 87 (2007) 1–11, https://doi.org/10.1002/bip.20762.
[3] G. Li, X.C. Zhang, GTP hydrolysis mechanism of Ras-like GTPases, J. Mol. Biol. 340 (2004) 921–932.
[4] R.A. Britton, Role of GTPases in bacterial ribosome assembly, Annu. Rev. Microbiol. 63 (2009) 155–176, https://doi.org/10.1146/annurev.micro.091208.073225.
[5] D.J. Bennison, S.E. Irving, R.M. Corrigan, The impact of the stringent response on TRAFAC GTPases and prokaryotic ribosome assembly, Cells 8 (2019) 1313.
[6] S. Goto, A. Muto, H. Himeno, GTPases involved in bacterial ribosome maturation, J. Biochem. (Tokyo) 153 (2013) 403–414.
[7] N. Upendra, K.M. Kavya, S. Krishnaveni, Molecular dynamics simulation studies on Bacillus subtilis RbgA: insights into the RbgA-ribosome association and GTPase activity, J. Biomol. Struct. Dyn. (2024) 1–11, https://doi.org/10.1080/07391102.2024.2444412.
[8] Y. Jeon, C.S. Ahn, H.J. Jung, H. Kang, G.T. Park, Y. Choi, J. Hwang, H.-S. Pai, DER containing two consecutive GTP-binding domains plays an essential role in chloroplast ribosomal RNA processing and ribosome biogenesis in higher plants, J. Exp. Bot. 65 (2014) 117–130.
[9] S. Majumdar, A. Acharya, S.K. Tomar, B. Prakash, Disrupting domain-domain interactions is indispensable for EngA-ribosome interactions, Biochim. Biophys. Acta BBA-Proteins Proteomics 1865 (2017) 289–303.
[10] O. Daumke, G.J.K. Praefcke, Invited review: mechanisms of GTP hydrolysis and conformational transitions in the dynamin superfamily, Biopolymers 105 (2016) 580–593, https://doi.org/10.1002/bip.22855.
[11] K. Kavya, N. Upendra, S. Krishnaveni, Conformational dynamics and ribosomal interactions of Bacillus subtilis Obg in various nucleotide-bound states: insights from molecular dynamics simulation, Int. J. Biol. Macromol. 279 (2024) 135337, https://doi.org/10.1016/j.ijbiomac.2024.135337.
[12] S.K. Tomar, N. Dhimole, M. Chatterjee, B. Prakash, Distinct GDP/GTP bound states of the tandem G-domains of EngA regulate ribosome binding, Nucleic Acids Res. 37 (2009) 2359–2370.
[13] N. Upendra, K. Kavya, S. Krishnaveni, Molecular dynamics simulation study on Bacillus subtilis EngA: the presence of Mg2+ at the active-sites promotes the functionally important conformation, J. Biomol. Struct. Dyn. 41 (2023) 9219–9231, https://doi.org/10.1080/07391102.2022.2151513.
[14] C. Da Silveira Tomé, A. Foucher, J. Jault, D. Housset, High concentrations of GTP induce conformational changes in the essential bacterial GTP ase EngA and enhance its binding to the ribosome, FEBS J. 285 (2018) 160–177, https://doi.org/10.1111/febs.14333.
[15] C. Eldin, C. Mélenotte, O. Mediannikov, E. Ghigo, M. Million, S. Edouard, J.-L. Mege, M. Maurin, D. Raoult, From Q fever to Coxiella burnetii infection: a paradigm change, Clin. Microbiol. Rev. 30 (2017) 115–190, https://doi.org/10.1128/CMR.00045-16.
[16] L. Guertler, U. Bauerfeind, J. Bluemel, R. Burger, C. Drosten, A. Groener, M. Heiden, M. Hildebrandt, B. Jansen, R. Offergeld, Coxiella burnetii–pathogenic agent of Q (query) fever, transfus, Med. Hemotherapy 41 (2013) 60.
[17] A. Bharat, J.E. Blanchard, E.D. Brown, A high-throughput screen of the GTPase activity of Escherichia coli EngA to find an inhibitor of bacterial ribosome biogenesis, SLAS Discov. 18 (2013) 830–836, https://doi.org/10.1177/1087057113486001.
[18] H.M. Berman, J. Westbrook, Z. Feng, G. Gilliland, T.N. Bhat, H. Weissig, I. N. Shindyalov, P.E. Bourne, The protein data bank, Nucleic Acids Res. 28 (2000) 235–242, https://doi.org/10.1093/nar/28.1.235.
[19] H. Berman, K. Henrick, H. Nakamura, Announcing the worldwide protein data bank, Nat. Struct. Mol. Biol. 10 (2003), https://doi.org/10.1038/nsb1203-980, 980–980.
[20] B. Webb, A. Sali, Comparative protein structure modeling using MODELLER, Curr. Protoc. Bioinform. 54 (2016) 5.6.1–5.6.37, https://doi.org/10.1002/cpbi.3.
[21] Z. Yang, K. Lasker, D. Schneidman-Duhovny, B. Webb, C.C. Huang, E.F. Pettersen, T.D. Goddard, E.C. Meng, A. Sali, T.E. Ferrin, UCSF chimera, MODELLER, and IMP: an integrated modeling system, J. Struct. Biol. 179 (2012) 269–278, https://doi.org/10.1016/j.jsb.2011.09.006.
[22] E.F. Pettersen, T.D. Goddard, C.C. Huang, G.S. Couch, D.M. Greenblatt, E.C. Meng, T.E. Ferrin, UCSF chimera—A visualization system for exploratory research and analysis, J. Comput. Chem. 25 (2004) 1605–1612, https://doi.org/10.1002/jcc.20084.
[23] M.J. Abraham, T. Murtola, R. Schulz, S. Páll, J.C. Smith, B. Hess, E. Lindahl, GROMACS: high performance molecular simulations through multi-level parallelism from laptops to supercomputers, SoftwareX 1–2 (2015) 19–25, https://doi.org/10.1016/j.softx.2015.06.001.
[24] S. Páll, A. Zhmurov, P. Bauer, M. Abraham, M. Lundborg, A. Gray, B. Hess, E. Lindahl, Heterogeneous parallelization and acceleration of molecular dynamics simulations in GROMACS, J. Chem. Phys. 153 (2020) 134110, https://doi.org/10.1063/5.0018516.
[25] H.J.C. Berendsen, D. Van Der Spoel, R. Van Drunen, GROMACS: a message-passing parallel molecular dynamics implementation, Comput. Phys. Commun. 91 (1995) 43–56, https://doi.org/10.1016/0010-4655(95)00042-E.
[26] J.A. Lemkul, From proteins to perturbed hamiltonians: a suite of tutorials for the GROMACS-2018 molecular simulation package [Article v1.0], Living J. Comput. Mol. Sci. 1 (2019), https://doi.org/10.33011/livecoms.1.1.5068, 5068–5068.
[27] B. Rizzuti, Molecular simulations of proteins: from simplified physical interactions to complex biological phenomena, Biochim. Biophys. Acta BBA - Proteins Proteomics 1870 (2022) 140757, https://doi.org/10.1016/j.bbapap.2022.140757.
[28] B.R. Brooks, R.E. Bruccoleri, B.D. Olafson, D.J. States, S. Swaminathan, M. Karplus, Charmm : a program for macromolecular energy, minimization, and dynamics calculations, J. Comput. Chem. 4 (1983) 187–217, https://doi.org/10.1002/jcc.540040211.
[29] J. Huang, S. Rauscher, G. Nawrocki, T. Ran, M. Feig, B.L. De Groot, H. Grubmüller, A.D. MacKerell, CHARMM36m: an improved force field for folded and intrinsically disordered proteins, Nat. Methods 14 (2017) 71–73, https://doi.org/10.1038/nmeth.4067.
[30] B.R. Brooks, C.L. Brooks, A.D. Mackerell, L. Nilsson, R.J. Petrella, B. Roux, Y. Won, G. Archontis, C. Bartels, S. Boresch, A. Caflisch, L. Caves, Q. Cui, A.R. Dinner, M. Feig, S. Fischer, J. Gao, M. Hodoscek, W. Im, K. Kuczera, T. Lazaridis, J. Ma, V. Ovchinnikov, E. Paci, R.W. Pastor, C.B. Post, J.Z. Pu, M. Schaefer, B. Tidor, R. M. Venable, H.L. Woodcock, X. Wu, W. Yang, D.M. York, M. Karplus, CHARMM: the biomolecular simulation program, J. Comput. Chem. 30 (2009) 1545–1614, https://doi.org/10.1002/jcc.21287.
[31] K. Vanommeslaeghe, E. Hatcher, C. Acharya, S. Kundu, S. Zhong, J. Shim, E. Darian, O. Guvench, P. Lopes, I. Vorobyov, A.D. Mackerell, CHARMM general force field: a force field for drug-like molecules compatible with the CHARMM all-atom additive biological force fields, J. Comput. Chem. 31 (2010) 671–690, https://doi.org/10.1002/jcc.21367.
[32] K. Vanommeslaeghe, A.D. MacKerell, Automation of the CHARMM general force field (CGenFF) I: bond perception and atom typing, J. Chem. Inf. Model. 52 (2012) 3144–3154, https://doi.org/10.1021/ci300363c.
[33] K. Vanommeslaeghe, E.P. Raman, A.D. MacKerell, Automation of the CHARMM general force field (CGenFF) II: assignment of bonded parameters and partial atomic charges, J. Chem. Inf. Model. 52 (2012) 3155–3168, https://doi.org/10.1021/ci3003649.
[34] A.D. MacKerell, D. Bashford, M. Bellott, R.L. Dunbrack, J.D. Evanseck, M.J. Field, S. Fischer, J. Gao, H. Guo, S. Ha, D. Joseph-McCarthy, L. Kuchnir, K. Kuczera, F.T. K. Lau, C. Mattos, S. Michnick, T. Ngo, D.T. Nguyen, B. Prodhom, W.E. Reiher, B. Roux, M. Schlenkrich, J.C. Smith, R. Stote, J. Straub, M. Watanabe, J. Wiórkiewicz-Kuczera, D. Yin, M. Karplus, All-atom empirical potential for molecular modeling and dynamics studies of proteins, J. Phys. Chem. B 102 (1998) 3586–3616, https://doi.org/10.1021/jp973084f.
[35] D.J. Price, C.L. Brooks, A modified TIP3P water potential for simulation with ewald summation, J. Chem. Phys. 121 (2004) 10096–10103, https://doi.org/10.1063/1.1808117.
[36] W.L. Jorgensen, J. Chandrasekhar, J.D. Madura, R.W. Impey, M.L. Klein, Comparison of simple potential functions for simulating liquid water, J. Chem. Phys. 79 (1983) 926–935, https://doi.org/10.1063/1.445869.
[37] G. Bussi, D. Donadio, M. Parrinello, Canonical sampling through velocity rescaling, J. Chem. Phys. 126 (2007) 014101, https://doi.org/10.1063/1.2408420.
[38] M. Parrinello, A. Rahman, Polymorphic transitions in single crystals: a new molecular dynamics method, J. Appl. Phys. 52 (1981) 7182–7190.
[39] T. Darden, D. York, L. Pedersen, Particle mesh ewald: an $N \cdot \log(N)$ method for ewald sums in large systems, J. Chem. Phys. 98 (1993) 10089–10092, https://doi.org/10.1063/1.464397.
[40] U. Essmann, L. Perera, M.L. Berkowitz, T. Darden, H. Lee, L.G. Pedersen, A smooth particle mesh ewald method, J. Chem. Phys. 103 (1995) 8577–8593, https://doi.org/10.1063/1.470117.
[41] B. Hess, H. Bekker, H.J.C. Berendsen, J.G.E.M. Fraaije, LINCS: a linear constraint solver for molecular simulations, J. Comput. Chem. 18 (1997) 1463–1472.
[42] W. Humphrey, A. Dalke, K. Schulten, VMD: visual molecular dynamics, J. Mol. Graph. 14 (1996) 33–38, https://doi.org/10.1016/0263-7855(96)00018-5.

[43] G.A. Tribello, M. Bonomi, D. Branduardi, C. Camilloni, G. Bussi, Plumed 2: new feathers for an old bird, Comput. Phys. Commun. 185 (2014) 604–613, https://doi.org/10.1016/j.cpc.2013.09.018.
[44] H.C. Jubb, A.P. Higueruelo, B. Ochoa-Montaño, W.R. Pitt, D.B. Ascher, T. L. Blundell, Arpeggio: a web server for calculating and visualising interatomic interactions in protein structures, J. Mol. Biol. 429 (2017) 365–371.
[45] H.K. Nagaraja rao, B. Poojary, K.K. Mohan Kumar, G. Chandrasehar, K. Sannathammegowda, A. Pandith, Novel isoxazolylpyrimidine derivatives: design, synthesis, antifungal activity and In-Silico studies, Asian J. Org. Chem. (2024) e202400021.
[46] A.E. García, Large-amplitude nonlinear motions in proteins, Phys. Rev. Lett. 68 (1992) 2696–2699, https://doi.org/10.1103/PhysRevLett.68.2696.
[47] A. Amadei, A.B. Linssen, H.J. Berendsen, Essential dynamics of proteins, Proteins 17 (1993) 412–425, https://doi.org/10.1002/prot.340170408.
[48] C.C. David, D.J. Jacobs, Principal component analysis: a method for determining the essential dynamics of proteins, Methods Mol. Biol. Clifton NJ 1084 (2014) 193–226, https://doi.org/10.1007/978-1-62703-658-0_11.
[49] R. Schulz, A.V. Vargiu, F. Collu, U. Kleinekathöfer, P. Ruggerone, Functional rotation of the transporter AcrB: insights into drug extrusion from simulations, PLoS Comput. Biol. 6 (2010) e1000806, https://doi.org/10.1371/journal.pcbi.1000806.
[50] U. N., K. and S., Molecular dynamics simulation study on Thermotoga maritima EngA: GTP/GDP bound state of the second G-domain influences the domain–domain interface interactions, J. Biomol. Struct. Dyn. 40 (2022) 1387–1399, https://doi.org/10.1080/07391102.2020.1826359.
[51] J. Eargle, Z. Luthey-Schulten, NetworkView: 3D display and analysis of protein·RNA interaction networks, Bioinformatics 28 (2012) 3000–3001, https://doi.org/10.1093/bioinformatics/bts546.
[52] A. Sethi, J. Eargle, A.A. Black, Z. Luthey-Schulten, Dynamical networks in tRNA: protein complexes, Proc. Natl. Acad. Sci. 106 (2009) 6620–6625, https://doi.org/10.1073/pnas.0810961106.
[53] N.M. Glykos, Software news and updates carma: a molecular dynamics analysis program, J. Comput. Chem. 27 (2006) 1765–1768, https://doi.org/10.1002/jcc.20482.
[54] M. Girvan, M.E.J. Newman, Community structure in social and biological networks, Proc. Natl. Acad. Sci. 99 (2002) 7821–7826, https://doi.org/10.1073/pnas.122653799.
[55] R.W. Floyd, Algorithm 97: shortest path, Commun. ACM 5 (1962) 345, https://doi.org/10.1145/367766.368168.
[56] W. Kabsch, C. Sander, Dictionary of protein secondary structure: pattern recognition of hydrogen-bonded and geometrical features, Biopolymers 22 (1983) 2577–2637, https://doi.org/10.1002/bip.360221211.
[57] L. Birnbaumer, A.R. Zurita, On the roles of Mg in the activation of G proteins, J. Recept. Signal Transduction 30 (2010) 372–375, https://doi.org/10.3109/10799893.2010.508165.